Quantum Many-Body Scars: Experimental Insights

Adrian Harkness[1], David Nizovsky[1], Caden Kacmarynski[1], Dmitrii Khitrin[1], and Xavier Moskala[1]

[1]Quantum Consortium: Case-Duke-Lehigh-Vandy Nexus, YQuantum2024 QuEra Challenge

April 2024

1 Introduction

The Eigenstate Thermalization Hypothesis (ETH) states that a chaotic quantum mechanical system prepared in an out-of-equilibrium state evolves towards thermal equilibrium. As the entropy of the system increases with time, all energy eigenstates should eventually be measured with equal probability. However, particular many-body wavefunctions have been found to violate the ETH by exhibiting periodic concentration in certain parts of the available Hilbert space [3]. This phenomenon is referred to as quantum many-body scarring, and it gives rise to controllable states with surprisingly long-lived coherence times.

In this project, we explore the weakly non-ergodic dynamics of quantum many-body scars in neutral-atom arrays. As opposed to strongly non-ergodic systems caused by integrability conditions or many-body localization, only some eigenstates in weakly non-ergodic systems behave atypically. As a result, the quantum dynamics of these systems depend strongly on their initial states [9].

We explore these dynamics using QuEra's Rydberg atom quantum computer simulator in analog mode. The Hamiltonian of the system is defined by

$$\frac{\mathcal{H}(t)}{\hbar} = \sum_i \frac{\Omega(t)}{2} \left(e^{i\phi(t)} |g_i\rangle \langle r_i| + e^{-i\phi(t)} |r_i\rangle \langle g_i| \right) - \sum_i \Delta(t)\hat{n}_i + \sum_{i<j} V_{ij}\hat{n}_i\hat{n}_j. \tag{1}$$

Here, $|g\rangle$ refers to the ground state of a qubit while $|r\rangle$ refers to the excited Rydberg state. The first term of equation 1 contains two time-dependent parameters, Rabi amplitude ($\Omega(t)$) and a complex phase ($\phi(t)$), and is off-diagonal in the computational basis making it responsible for driving the qubits between ground and excited states. The second term contains the time dependent detuning $\Delta(t)$ that can be used to dictate the ground state of the system. The

third term V_{ij} dictates the repulsive Van der Waals interactions, proportional to $\frac{1}{d^6}$, between qubit pairs [1].

We choose the spacings between lattice cites such that Nearest Neighbor interactions $V_0 > \Omega$ prevent neighboring atoms from both occupying the $|r\rangle$ state. This is referred to as a Rydberg Blockade. Specifically, we explore bipartite lattices prepared in the ground state $|G\rangle = |ggg...\rangle$ and evolved adiabatically to the antiferromagnetic state $|AF_1\rangle$ (e.g. 1D spin chains in the state $|rgrg...\rangle$) during state preparation. We then rapidly quench the system at fixed Ω to a small detuning and observe the system evolve to a disordered state. While this is expected of a system approaching thermal equilibrium, the system unexpectedly continues evolving to the opposite antiferromagnetic state $|AF_2\rangle$. Given more time, the system then evolves back to $|AF_1\rangle$ and repeats its periodic behavior while naturally losing coherence.

We use quantum simulators to examine how different lattice geometries exhibit different scarring probabilities, finding that 1D chain lattices and 2D honeycomb lattices exhibit the most pronounced scarring. We also implement time-dependent and time-independent detuning schedules during quenching, showing that time-dependent periodic detuning greatly improves the scarring lifetime and allows for careful engineering of scarring frequency. Lastly, we find that our scarring probabilities improve when implementing a readout error mitigation technique.

2 Simulations

In this section, we demonstrate simulations showing quantum scars for different atomic array structures. All tasks were performed with 200 shots each.

2.1 Chain

The simplest example of a quantum structure is a 1D chain, and [3] shows numerical evidence that 1D chains also maintain the longest scarring lifetimes among 1D and 2D arrays. We start with simulating the time evolution of 13-qubit chain under $\mathcal{H}(t)$ with constant Rabi frequency and linearly growing detuning (as suggested in the Bloqade tutorial [7]). As the result of state preparation, around 80% of the time, our chain ends up in $|AF_1\rangle$ as shown in figure 1. The periodic return to the $|AF_1\rangle$ state during quenching is shown in figure 2.

Next, we proceed to emulate the chain model under the drive of oscillating Rabi frequency during quenching, as shown in figure 4. The probability of $|AF_1\rangle$ being occupied for this case is showed in plot **??**, showing a much improved scarring lifetime. With a driving frequency of $\omega_d = 10^6$ Hz, we observe that the scarring revival frequency decreases to $\omega_s = .5 * 10^6$. This agrees with theory provided in [3] that the scarring lifetime with a detuning driving frequency increases, and the scarring frequency changes to $\frac{\omega_d}{2}$. This supports that the dynamics of quantum many-body scarring can be carefully manipulated for a range of different applications.
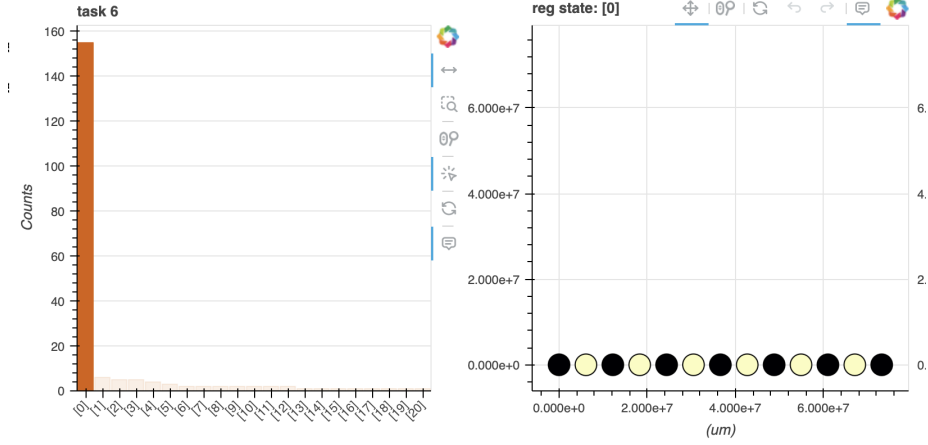
Figure 1: [Left] Number of counts for each initialized state, most likely state highlighted [Right] Chain configuration of the most likely state $|AF_1\rangle$.
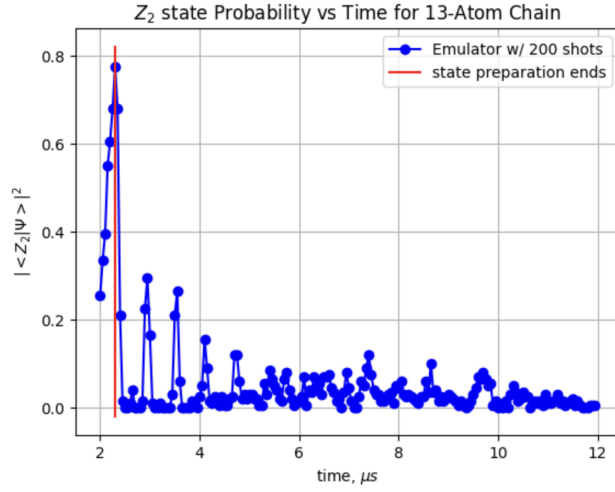

Figure 2: $|AF_1\rangle$ occupancy over time for a 13-atom chain with constant Rabi frequency

2.2 Quasi Circle

Inspired by solid state methods of enforcing periodic boundary conditions as well as Rydberg quantum wires used to propagate entanglement[6], this structure (figure 6) is of particular interest since it can be used as a basis for more complex topological configurations. The chain of 6 atoms is a familiar configuration; however, the first atom is connected to the last one via quantum wire
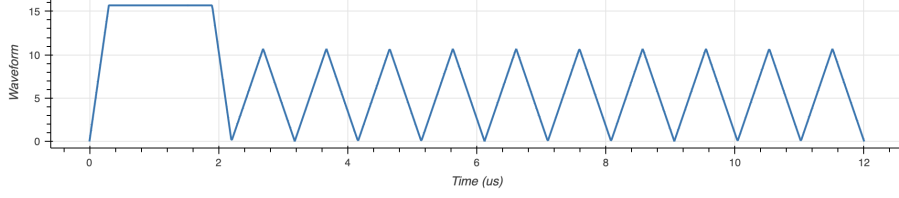
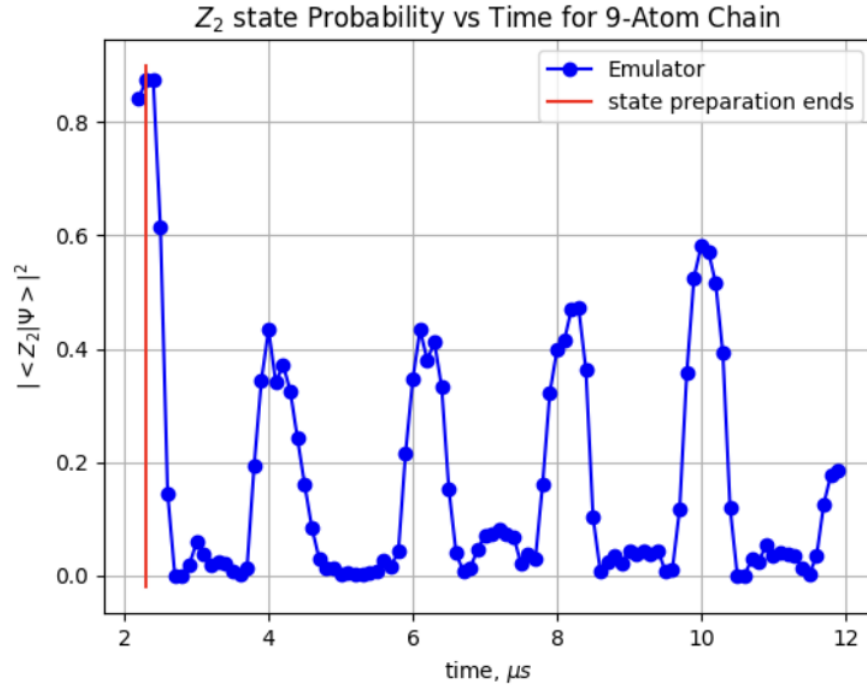Figure 3: Rabi frequency waveform for 9-atom chain experiment

Figure 4: $|AF_1\rangle$ occupancy over time for a 9-atom chain with Rabi frequency driven at ω_d. The frequency of the scarring changes to $\frac{\omega_d}{2}$.

formed with 6 auxiliary qubits. One could think of this structure as a closed interval $[a, b]$ equipped with an equivalence relation $\sim$: $a \sim b$. Just as $[a, b]/\sim$ is homeomorphic to S^1 and is in some ways similar to an infinite chain, our quasi-circle forms a two-dimensional loop. Importantly, the choice to not create an explicit circle, where all points are equidistant from the center, conserves more space allowing for the implementation of other structures or complicating the existing structure with much more ease and feasibility. Utilizing quantum wires technique further, shapes such as a cylinder, hypercube, or torus can be

4

embedded in the 2D plane of an atomic trap.

We find that the decay rate of scarring is higher in the quasi circle than in the 1D array, and state-preparation success probability is significantly lower at around 20%.
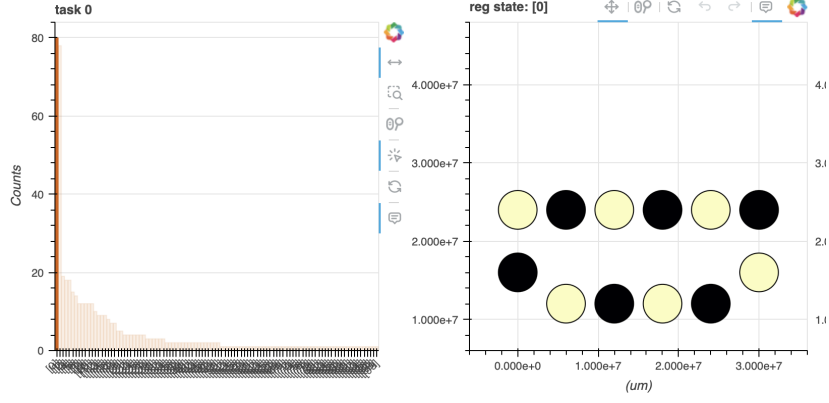

Figure 5: The quasi-circle structure with corresponding $|AF_1\rangle$ state
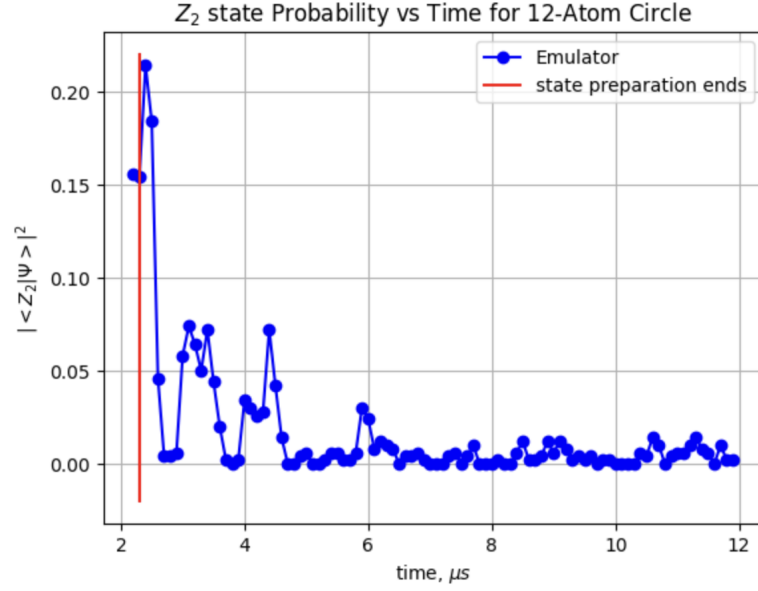

Figure 6: Occupation probability of the $|AF_1\rangle$ state.

2.3   Square

Following the geometries demonstrated in [3], we implement a nine qubit square array with a checkerboard pattern as the antiferromagnetic state. In contrast to [3], we see that the decay rate of the scarring is actually lower in the square configuration than in the 1D chain. We also observe that state-preparation success probability is significantly lower at around 20%.
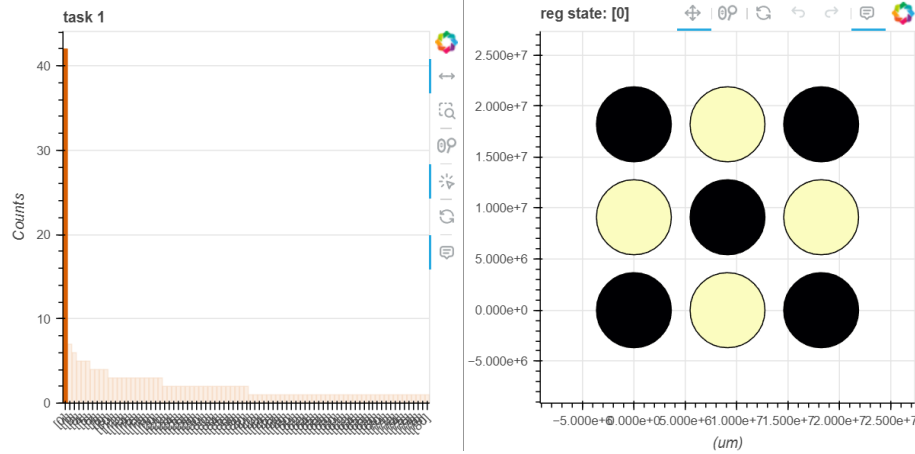

Figure 7: The square structure with corresponding $|AF_1\rangle$ state

2.4   Honeycomb

We continue experimentally demonstrating the geometries explored in [3] by implementing a ten qubit honeycomb array. In contrast to [3], we again see that the decay rate of the scarring is actually lower in the honeycomb configuration than in the 1D chain. We also observe that state-preparation success probability is lower at around 55%.

2.5   Decay Rate Comparison

We fit the peaks of the data from our plots of the Z_2 state probability vs time for each system to an exponential function with the decay rate as a parameter. As one can see in figure 11 and table 1, we get some relatively unexpected results. The driven versions of the square, circle, and honeycomb system all decay faster than their non-driven counterpart, in most cases by almost a factor of two. This could indicate that in these 2D systems that the simulator would suggest that these geometries do not actually do better with an oscillating Ω, but we have much concern with our ability to fit the simulated results as in some cases the decays are clearly non-exponential and in the worst cases the envelope of the decay begins to increase after some time. We find agreement
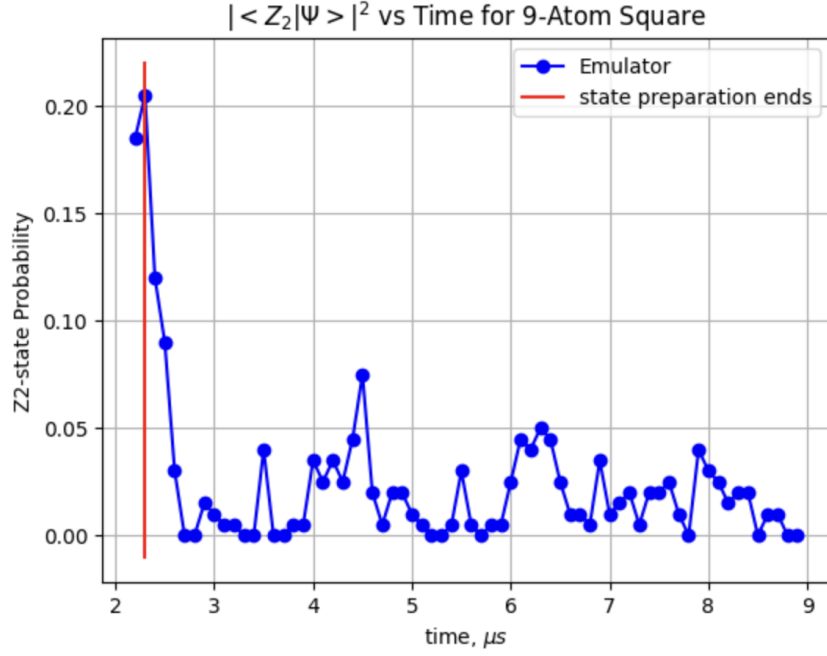
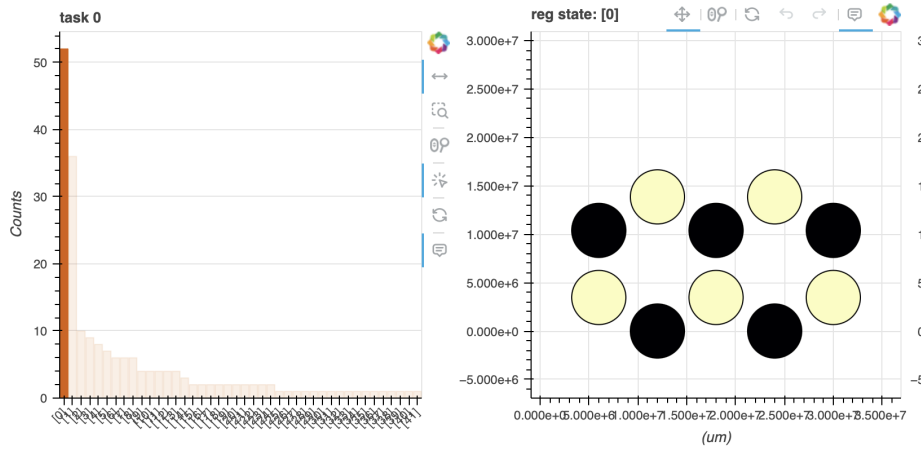Figure 8: Occupation probability of the $|AF_1\rangle$ state.

Figure 9: The honeycomb structure with corresponding $|AF_1\rangle$ state

with reference [3]'s figure 3B, as the driven chain decays slower than the normal chain, but we did not run them for the same number of atoms so they may not be directly comparable. Additionally, we find that the HoneyComb and
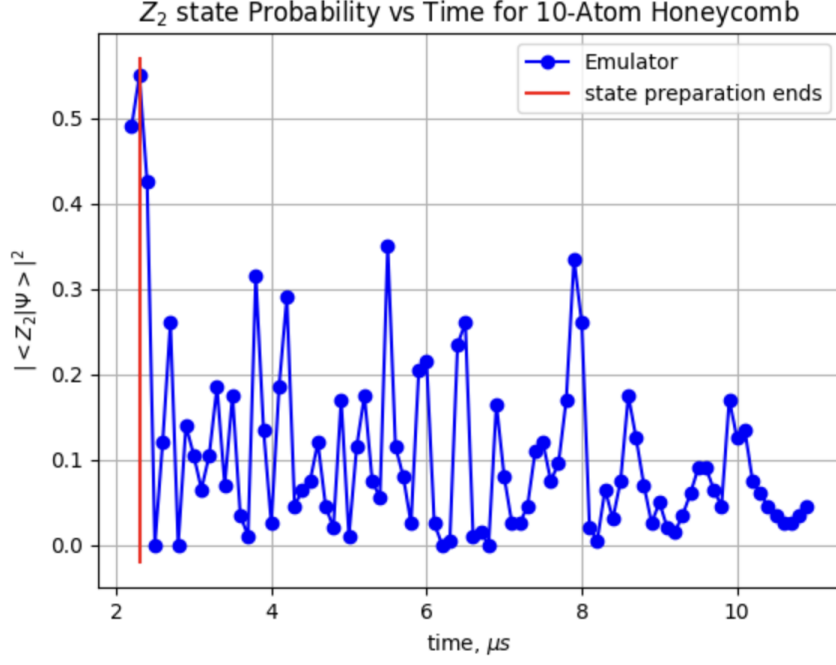
Figure 10: Occupation probability of the $|AF_1\rangle$ state.

Table 1: Fitted Decay Rates of the Systems

System	Decay Rate in MHZ ± 0.05
13-Atom Chain	0.86
9-Atom Chain (driven)	0.06
9-Atom Square	0.18
9-Atom Square (driven)	0.50
10-Atom Circle	0.32
10-Atom Circle (driven)	0.69
10-Atom HoneyComb	0.12
10-Atom HoneyComb (driven)	0.26

Square lattice decays much slower than the 13-Atom Chain which is in clear disagreement with reference [3]. Once again, we would attribute this to the statistics of fitting to the data, which could possibly be resolved with more and higher fidelity data or might be a limitation of the simulation that we've somehow run into. More work is needed to address this concern.
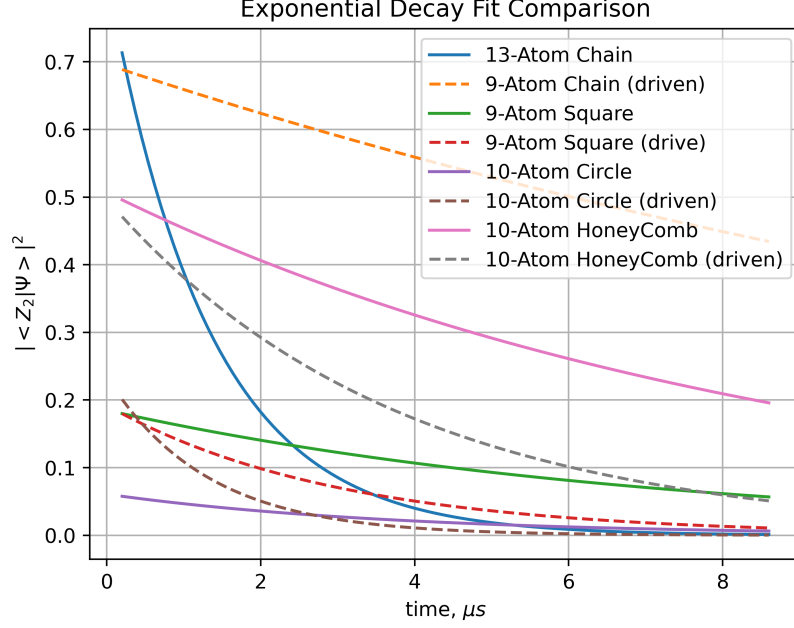
Figure 11: Comparison between the exponential fits of the various geometries.

3 Hardware

Error 404: Hardware not found

4 Readout Error Mitigation

In the context of neutral atom quantum computing, the readout process is a critical stage where the quantum state of each atom is measured. The readout involves detecting whether an atom is in its ground state or a Rydberg state. However, this process is prone to errors such as decay of the Rydberg state during measurement, or the failure to excite the atom to the Rydberg state due to technical imperfections or environmental decoherence. These errors can lead to an incorrect readout, either by falsely identifying a ground state atom as a Rydberg atom or vice versa. To mitigate these errors, we adopt a confusion matrix approach to adjust the experimental readout probabilities to better reflect the true state probabilities.

The confusion matrix, denoted as C, is a square matrix that represents the conditional probabilities of recording an experimental outcome e given the true quantum state t. This matrix is formalized as:

$$C = \begin{pmatrix} P(e_0|t_0) & P(e_0|t_1) \\ P(e_1|t_0) & P(e_1|t_1) \end{pmatrix}$$

where the matrix elements $C_{ij} = P(e_i|t_j)$ are directly obtained from experimental data.

Given a quantum system with two states, we express the true state probabilities as a column vector:

$$P_t = \begin{pmatrix} P(t_0) \\ P(t_1) \end{pmatrix}$$

Similarly, the experimentally measured state probabilities are represented as:

$$P_e = \begin{pmatrix} P(e_0) \\ P(e_1) \end{pmatrix}$$

The relationship between the experimental and theoretical probabilities is given by the equation:

$$P_e = C \cdot P_t$$

By measuring the experimental probabilities and knowing the theoretical predictions, we construct the confusion matrix which encapsulates the error characteristics of the readout process. The primary objective is then to estimate the true state probabilities, which can be computed by inverting the confusion matrix:

$$P_t = C^{-1} \cdot P_e$$

In the context of the provided matrix, the inversion process yields the theoretical probabilities corrected for readout errors. However, the inversion is contingent upon C being a non-singular matrix. In cases where C is not invertible or is poorly conditioned, regularization techniques such as Tikhonov regularization or the Moore-Penrose pseudoinverse could be employed to stabilize the inversion.

We employ the Moore-Penrose pseudoinverse, denoted as C^+, which serves as a generalization of the matrix inverse for non-square matrices or matrices that are not full rank. Once C is estimated, the pseudoinverse C^+ only needs to be computed once. This facilitates the Readout Error Mitigation (REM) process by applying C^+ to the measurement outcomes to correct for the readout errors.

The raw experimental results, denoted by the bitstrings, are converted into a probability vector p, representing the empirical probability distribution of the system's readout states. After obtaining C^+, we apply it to p to compute the adjusted quasi-probability distribution:

$$p' = C^+ \cdot p$$

This resulting vector p' might not be a legitimate probability distribution as it can contain negative entries. To rectify this, we seek the closest positive probability distribution [4] p'' by solving the optimization problem:

$$p'' = \min_{p_{\text{positive}}} \|p' - p_{\text{positive}}\|_1$$

Upon computing p'', we then sample from this new distribution to obtain a set of outcomes that more accurately reflects the true state of the quantum system. These samples are used as the basis for our mitigated results, allowing us to draw conclusions about result probabilities (figure 12).
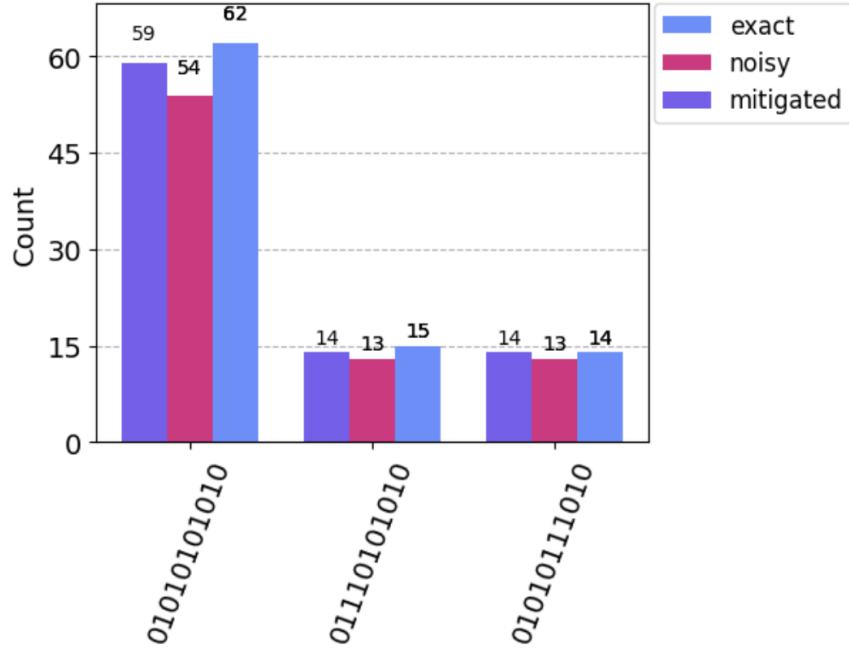
Figure 12: Example of error mitigation. Only three states with the highest probabilities are left for demonstration

5   Conclusion

We demonstrate quantum many-body scarring in 1D and 2D Rydberg atom arrays by preparing the antiferromagnetic $|AF_1\rangle$ state in various geometries. The characteristic mark of scarring is a periodic occupation of $|AF_1\rangle$ and $|AF_2\rangle$ states, which we observe in all tested geometries.

State preparation is most efficient in a 1D lattice array at 80% probability of success, while we see significantly lower success probabilities for other configurations. Further exploration could be done to optimize adiabatic annealing schedules for different geometries to efficiently prepare the antiferromagnetic state from the ground state.

We also examine the effect of driving the detuning parameter at a frequency ω_d during quenching in comparison to maintaining a fixed detuning parameter. In the 1D configuration, oscillating the detuning parameter increases the lifetime of quantum scarring while changing the scarring frequency to $\frac{\omega_d}{2}$. However, we see that driving the detuning parameter actually decreases the scarring lifetime of other lattice geometries. More data and better models are needed to conclusively determine the effect of driven detuning on scarring lifetimes. Further study of this effect could up possibilities to fine-tune the scarring dynamics of quantum many-body systems for specific applications.

Lastly, we implement a readout error mitigation strategy and see consistent improvement over noisy unmitigated results. Through the computation of the Moore-Penrose pseudoinverse of the confusion matrix, we have implemented a method to mitigate readout errors and approximate the true quantum state probabilities. We discovered that the REM approach is both practical and robust, offering a scalable solution to reduce the impact of noise in quantum computation experiments on existing quantum hardware.

References

[1] QuEra Qbook. https://qbook.quera.com/. Accessed on April 14, 2024.

[2] H. Bernien, S. Schwartz, A. Keesling, H. Levine, A. Omran, H. Pichler, S. Choi, A. S. Zibrov, M. Endres, M. Greiner, et al. Probing many-body dynamics on a 51-atom quantum simulator. *Nature*, 551(7682):579–584, 2017.

[3] D. Bluvstein, A. Omran, H. Levine, A. Keesling, G. Semeghini, S. Ebadi, T. T. Wang, A. A. Michailidis, N. Maskara, W. W. Ho, et al. Controlling quantum many-body dynamics in driven rydberg atom arrays. *Science*, 371(6536):1355–1359, 2021.

[4] S. Bravyi, S. Sheldon, A. Kandala, D. C. Mckay, and J. M. Gambetta. Mitigating measurement errors in multiqubit experiments. *Physical Review A*, 103(4), 2021.

[5] S. Bravyi, S. Sheldon, A. Kandala, D. C. Mckay, and J. M. Gambetta. Mitigating measurement errors in multiqubit experiments. *Physical Review A*, 103(4):042605, 2021.

[6] M. Kim, K. Kim, J. Hwang, E.-G. Moon, and J. Ahn. Rydberg quantum wires for maximum independent set problems. *Nature Physics*, 18(7):755–759, 2022.

[7] QuEra Computing Inc. Quantum scar dynamics. Neutral Atom SDK Documentation, 2023. Accessed: 2024-04-14.

[8] J. Smith and S. Johnson. Example article. *Journal of Examples*, 10(2):100–120, 2020.

[9] C. J. Turner, A. A. Michailidis, D. A. Abanin, M. Serbyn, and Z. Papić. Weak ergodicity breaking from quantum many-body scars. *Nature Physics*, 14(7):745–749, 2018.

Appendix

Exponential Fits

Exponential Decay Fit of 13-Atom Chain

Exponential Decay Fit of 9-Atom Square

Exponential Decay Fit of 9-Atom Square (driven)

14

Exponential Decay Fit of 10-Atom Circle

Exponential Decay Fit of 10-Atom Circle (driven)

Exponential Decay Fit of 10-Atom HoneyComb

Exponential Decay Fit of 10-Atom HoneyComb (driven)

16